Available online at www.sciencedirect.com

ScienceDirect

International Journal of Solids and Structures 44 (2007) 1844–1862

INTERNATIONAL JOURNAL OF SOLIDS and STRUCTURES

www.elsevier.com/locate/ijsolstr

Modeling of ductile fracture: Application of the mechanism-based concepts

Jinkook Kim, Guihua Zhang, Xiaosheng Gao *

Department of Mechanical Engineering, The University of Akron, Akron, OH 44325, USA

Received 9 April 2006; received in revised form 24 August 2006
Available online 1 September 2006

Abstract

This paper summarizes our recent studies on modeling ductile fracture in structural materials using the mechanism-based concepts. We describe two numerical approaches to model the material failure process by void growth and coalescence. In the first approach, voids are considered explicitly and modeled using refined finite elements. In order to predict crack initiation and propagation, a void coalescence criterion is established by conducting a series of systematic finite element analyses of the void-containing, representative material volume (RMV) subjected to different macroscopic stress states and expressed as a function of the stress triaxiality ratio and the Lode angle. The discrete void approach provides a straightforward way for studying the effects of microstructure on fracture toughness. In the second approach, the void-containing material is considered as a homogenized continuum governed by porous plasticity models. This makes it possible to simulate large amount of crack extension because only one element is needed for a representative material volume. As an example, a numerical approach is proposed to predict ductile crack growth in thin panels of a 2024-T3 aluminum alloy, where a modified Gologanu–Leblond–Devaux model [Gologanu, M., Leblond, J.B., Devaux, J., 1993. Approximate models for ductile metals containing nonspherical voids – Case of axisymmetric prolate ellipsoidal cavities. J. Mech. Phys. Solids 41, 1723–1754; Gologanu, M., Leblond, J.B., Devaux, J., 1994. Approximate models for ductile metals containing nonspherical voids – Case of axisymmetric oblate ellipsoidal cavities. J. Eng. Mater. Tech. 116, 290–297; Gologanu, M., Leblond, J.B., Perrin, G., Devaux, J., 1995. Recent extensions of Gurson's model for porous ductile metals. In: Suquet, P. (Ed.) Continuum Micromechanics. Springer-Verlag, pp. 61–130] is used to describe the evolution of void shape and void volume fraction and the associated material softening, and the material failure criterion is calibrated using experimental data. The calibrated computational model successfully predicts crack extension in various fracture specimens, including the compact tension specimen, middle crack tension specimens, multi-site damage specimens and the pressurized cylindrical shell specimen.

Keywords: Void growth and coalescence; Discrete voids; Porous continuum model; Stress triaxiality; Lode parameter; Ductile crack growth; Thin specimens

* Corresponding author. Tel.: +1 330 972 2415; fax: +1 330 972 6027.
E-mail address: xgao@uakron.edu (X. Gao).

0020-7683/$ - see front matter
doi:10.1016/j.ijsolstr.2006.08.028

1. Introduction

Engineering structures inevitably contain microscopic defects or crack-like flaws arising from the manufacture and operation processes. These defects and flaws can grow and propagate in the structure under combined loading and environmental conditions, leading to catastrophic failure. Fracture mechanics, which connects material science and solid mechanics, seeks to provide quantitative methodologies to evaluate how microscopic defects and structural flaws affect the behavior and integrity of structural components. The current and future significance of a known or postulated population of defects is determined by comparing the material's resistance to further damage with the driving force for crack propagation caused by the operating conditions (temperature, loading mode, loading rate, environment, etc.). In a typical analysis, the driving force is estimated using analytical tools while the material resistance to fracture (''toughness'') is measured using laboratory tests on standard (small) specimens (Anderson, 1994). However, the complex material separation process depends strongly on the local stress and deformation fields, and therefore, differences in geometry, size, crack configuration, loading condition, etc. between actual structural components and laboratory test specimens complicate greatly the notions of crack driving force and material resistance to crack propagation. The success of fracture mechanics lies in its ability to combine a theoretical framework with experimentally measured critical quantities (Hutchinson and Evans, 2000).

Mechanism-based concepts provide key insights for development of ''transferable'' fracture mechanics models for damage assessment. Ductile fracture in metallic alloys usually follows a multistep failure process involving several interacting, simultaneous mechanisms (Van Stone et al., 1985; Garrison and Moody, 1987): (1) nucleation of microvoids by fracture or decohesion of second-phase inclusions, (2) growth of voids induced by plastic straining, (3) localization of plastic flow between the enlarged voids, and (4) final tearing of the ligaments between enlarged voids. Nucleation of voids from large inclusions generally occurs at relatively low stress levels, and therefore, voids are often assumed to be present in the material at the onset of loading. The final material separation process usually proceeds very rapidly and is often facilitated by nucleation and growth of secondary microvoids. Based on the fracture mechanism, a straight-forward approach to simulate the ductile failure process is to model individual voids explicitly using refined finite elements, e.g., Aravas and McMeeking (1985a,b), Hom and McMeeking (1989), Tvergaard and Hutchinson (2002), Kim et al. (2003) and Gao et al. (2005). A distinct advantage of this approach is the exact implementation of the void growth behavior. It provides an effective method to study the mechanisms of ductile fracture and to analyze the trends of fracture toughness (Pardoen and Hutchinson, 2003; Gao et al., 2005).

The idea of the discrete void approach is very simple. However, it would require a huge number of elements to model crack extension in a structural component. Such a finite element model is far beyond the current computational capability. As a practical alternative, the porous continuum approach provides an effective means to predict extensive crack propagation. Various forms of porous material models have been developed to describe void growth and the associated macroscopic softening during the fracture process. The Gurson–Tvergaard (GT) porous plasticity model (Gurson, 1977; Tvergaard, 1981, 1982), which assumes voids are spherical in materials and remain spherical in the growth process, has been widely used in modeling the ductile failure process and ductile crack extension (Xia et al., 1995; Ruggieri et al., 1996; Gao et al., 1998a,b). But many processed materials, such as rolled plates, have non-spherical voids. And even for materials having initially spherical voids, the voids will change to prolate or oblate shape after deformation, depending on the state of the applied stress. In order to overcome these difficulties, Gologanu et al. (1993, 1994, 1995) derived a yield function for materials containing spheroidal voids. During plastic deformation, both the volume fraction and the shape of voids evolve as deformation increases. Since non-spherical voids are considered in the constitutive model, preferred material orientation exists and the plastic behavior becomes anisotropic. Kim and Gao (2005) recently proposed a method to formulate the consistent tangent modulus for general plasticity models, which is required for preserving the quadratic convergence rate of the global Newton iterations in the solution of the incremental problem. Using this method, the Gologanu–Leblond–Devaux (GLD) model, although having a very complicated form, can be easily implemented into the finite element code. The GLD model provides an important improvement to the widely adopted GT model in describing void growth and the corresponding material behavior during the ductile fracture process (Pardoen and Hutchinson, 2000, 2003; Benzerga, 2002; Benzerga et al., 2004; Gao and Kim, 2006).

Since the time of Bridgman (1952), the interest of the fracture mechanics community has been focused on the effect of the hydrostatic stress on fracture. In literature, the stress triaxiality ratio, defined as the ratio of the hydrostatic stress to the equivalent stress, is often used as the sole parameter to characterize the effect of the triaxial stress state on ductile fracture. However, multiple stress states with different principal stress values can result in the same stress triaxiality ratio. Recent studies by Kim et al. (2003, 2004), Gao et al. (2005) and Gao and Kim (2006), found that the macroscopic stress–strain response and the void growth and coalescence behavior of the voided RMV are different for each stress state even though the stress triaxiality ratio remains the same. Therefore, another parameter, e.g., the Lode parameter, should be introduced to distinguish stress states having the same triaxiality ratio. Kim et al. (2003, 2004), Gao et al. (2005) and Gao and Kim (2006) have demonstrated the significant effects of the Lode parameter on the ductile fracture process. Wierzbicki and Xue (2005) address this issue with a similar approach by proposing a ductile failure criterion as a function of both the first and third stress invariants.

This paper discusses both the discrete void approach and the porous continuum approach to model ductile fracture. We consider the occurrence of material failure (void coalescence) to be when localization of plastic flow takes place in the inter-void ligament (Koplik and Needleman, 1988) and we obtain the failure criterion as a function of the stress triaxiality ratio and the Lode angle by conducting systematic finite element analyses of the void-containing RMV subjected to different macroscopic stress states. Using the small scale yielding (SSY), boundary layer model (Rice, 1974) with discrete voids represented in the crack tip region by refined finite element mesh, two void growth mechanisms, void-by-void growth and multiple void interaction, are studied. With the material failure criterion obtained from unit cell analyses, the effects of the initial relative void spacing, void pattern, void shape and void volume fraction on ductile fracture toughness are investigated. Finally, a numerical approach is proposed to predict ductile crack growth in thin panels of a 2024-T3 aluminum alloy, where the GLD model is used to describe the void growth process and the material failure criterion is calibrated using experimental data. The calibrated computational model is applied to predict crack extension in specimens having various initial crack configurations and the numerical predictions agree very well with experimental measurements.

2. Modeling ductile fracture using explicit void representation

This section presents a computational approach to model ductile fracture using explicit void representation. An array of voids ahead of the crack front is explicitly modeled using refined finite elements to understand the nature of void growth and different ductile failure mechanisms. A crack initiation and growth criterion is established based on the results of extensive unit cell analyses. And finally, the effects of the initial relative void spacing, void pattern, void shape and void volume fraction on ductile fracture toughness are discussed.

2.1. The SSY boundary layer model

The small scale yielding (SSY), boundary layer model simplifies the generation of numerical solutions for crack problems. Here it assumes that the plastic zone size is small comparing to the geometric dimensions of the specimen. Fig. 1(a) shows a periodical distribution of voids in the plane of crack propagation. In an attempt to rationalize fracture behavior, a local coordinate system is set up such that the x-axis represents the crack propagation direction, the y-axis represents the crack opening direction and the z-axis represents the thickness direction. Considering the existence of symmetry about the crack plane, only half of the region needs to be modeled. Except near free surfaces the deformation in the thickness direction can be assumed periodically symmetric. Neglecting the free surface effect allows us to apply the periodic boundary conditions and consider half of the void spacing distance in the thickness direction only, Fig. 1(b).

Fig. 2 (a) shows a typical finite element mesh of the SSY model. Close-up of the crack tip region is shown in Fig. 2(b) and (c) for finite element modeling containing one row and two rows of voids, respectively. A typical mesh containing two rows of voids consists of 18,000 20-node, isoparametric, brick elements (86,000 nodes) with reduced integration. With the assumption of the periodic void distribution, it is natural to consider the material ahead of the crack front as an array of unit cells with each unit cell containing a void at its center. The ratio of the void volume to the volume of the cell (including the void) defines the void volume fraction of

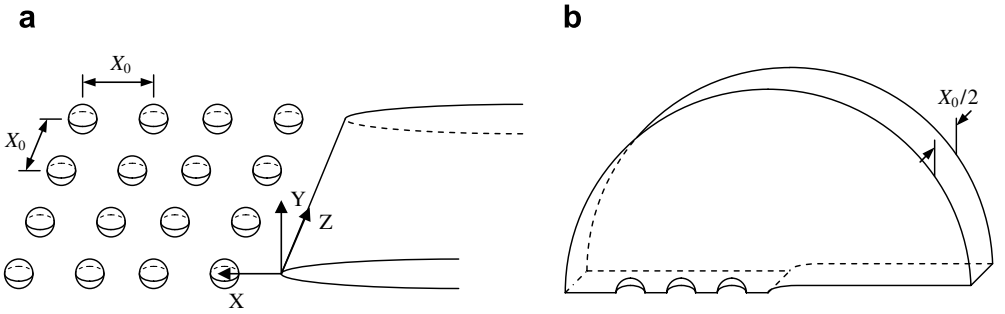

Fig. 1. (a) Periodical distribution of voids in the plane of crack propagation. (b) Domain of the boundary value problem.

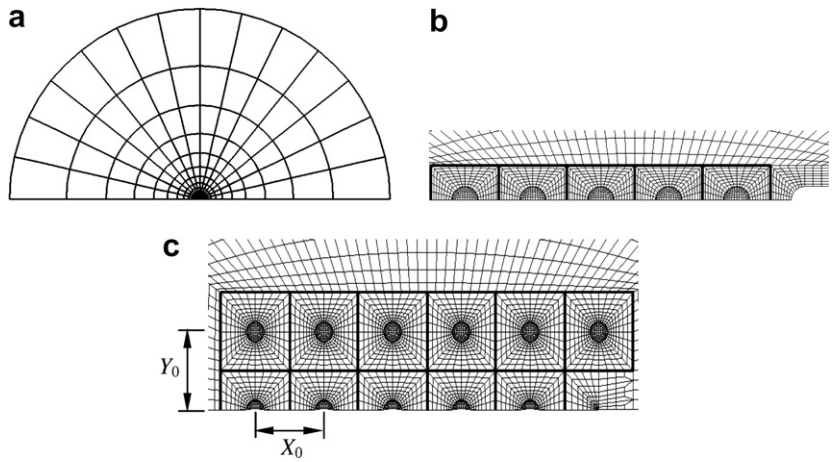

Fig. 2. (a) A typical finite element mesh of the SSY model. (b) Close-up of the crack tip region containing a row of five voids. (c) Close-up of the crack tip region containing two rows of voids.

the material. To resolve the crack tip deformation field and enhance convergence of the nonlinear iterations, the finite element mesh contains an initial root radius at the crack tip. numerical solutions are generated by imposing displacements of the elastic, asymptotic mode I field (plane strain) on the outer circular boundary.

Three types of initial void shapes, spherical shape, prolate shape, and oblate shape, are considered. Fig. 3 shows the geometrical representation of the voids. The prolate and oblate voids are assumed to be axisymmetric about the y-axis and an initial aspect ratio is defined as $W_0 = R_{0y}/R_{0x}$. Therefore, $W_0 = 1$ corresponds to the spherical shape, $W_0 > 1$ corresponds to the prolate shape, and $W_0 < 1$ corresponds to the oblate shape.

Several initial void arrangements are considered in this study. The spacing between adjacent voids in the crack propagation direction is denoted as X_0, which is the same as the distance from the first void to the crack

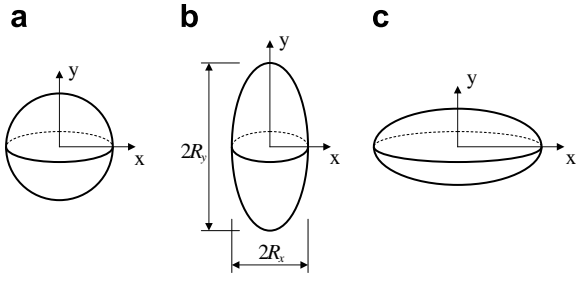

Fig. 3. Geometric representation of voids: (a) spherical void, (b) prolate void, and (c) oblate void.

tip. The distance between two adjacent rows of voids is denoted as Y_0. A parameter λ_0 is defined as the ratio of the void spacing in the y-direction to the void spacing in the x-direction, $\lambda_0 = Y_0/X_0$, measuring the relative void spacing. The initial void volume fraction is computed as $f_0 = 4\pi R_x^2 R_y/(3X_0^2 Y_0)$. The numerical analyses in this study are carried out using the finite element program ABAQUS (2001), which employs a finite strain and an updated Lagrangian formulation.

2.2. Two void growth mechanisms

Our analyses confirm the existence of two distinct void growth mechanisms, i.e., void-by-void growth mechanism for materials containing small initial void volume fractions and multiple void interaction mechanism for materials containing large initial void volume fractions. As an example, Fig. 4 shows the deformed meshes for two models each containing one row of initially spherical voids. The initial void volume fraction values are $f_0 = 0.0013$ and 0.014, respectively. The material chosen for this analysis has a Young's modulus (E) of 200 GPa, Poisson's ratio (ν) of 0.3 and yield stress (σ_0) of 600 MPa and obeys a power-law hardening (true) stress–strain relation with the hardening exponent $N = 0.1$. The deformed mesh of the $f_0 = 0.0013$ model at an applied load level of $J/(X_0\sigma_0) = 2.73$ is shown in Fig. 4(a) and the deformed mesh of the $f_0 = 0.014$ model at an applied load level of $J/(X_0\sigma_0) = 0.98$ is shown in Fig. 4(b), where J is Rice's J-integral. In Fig. 4(a), only the first void from the crack tip has significant volume increase while in Fig. 4(b), the volumes of several voids increase simultaneously.

Our further analyses reveal that, besides the initial void volume fraction, other factors also affect the void growth mechanism when the initial void volume fraction is large. Existence of the second row of voids as shown in Fig. 2(c) reduces the interaction among voids on the crack growth plane and delays the transition from void by void growth mechanism to multiple voids interaction mechanism. Increase of λ_0 (relative void spacing) intensifies the interaction among neighboring voids and facilitates the transition from void-by-void growth mechanism to multiple void interaction mechanism. A change of the void distribution pattern by shifting the positions of second row voids does not affect the growth rates of voids in the plane of crack propagation. Our results also show that when other parameters are the same, the oblate void grows faster than the spherical void and the spherical void grows faster than the prolate void.

2.3. Void coalescence criterion

In order to simulate crack formation and propagation, a criterion for void coalescence is required. After the onset of void coalescence, the material loses load carrying capacity rapidly. The criterion for onset of void coalescence can be obtained by conducting systematic finite element analyses of the void-containing RMV subjected to different macroscopic stress states. Consider a RMV containing a void at its center and subjected to the macroscopic stresses Σ_1, Σ_2 and Σ_3. The stress triaxiality ratio is defined as

$$T = \frac{\Sigma_h}{\Sigma_e}, \tag{1}$$

where Σ_h and Σ_e represent the hydrostatic stress and the equivalent stress, respectively, and the Lode angle is defined by

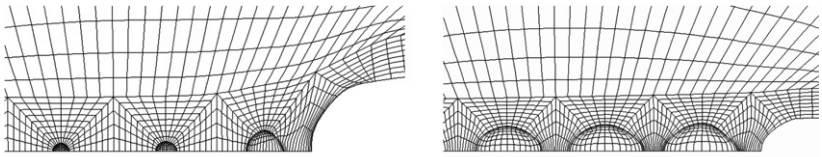

(a) $f_0 = 0.0013$ (b) $f_0 = 0.014$

Fig. 4. Deformed finite element meshes showing two distinct void growth mechanisms.

$$\tan\theta = \frac{2\Sigma_3 - \Sigma_2 - \Sigma_1}{\sqrt{3}(\Sigma_2 - \Sigma_1)}. \tag{2}$$

Kim et al. (2003, 2004), Gao et al. (2005) and Gao and Kim (2006) have demonstrated that both the stress triaxiality ratio and the Lode parameter have significant effects on the ductile failure process. Therefore, boundary conditions on the outer surfaces of the RMV are prescribed such that the macroscopic parameters T and θ are kept constant during the entire deformation history. By introducing two stress ratios, $\rho_1 = \Sigma_1/\Sigma_2$ and $\rho_2 = \Sigma_3/\Sigma_2$, the nonlinear constraints equations for the three-dimensional stress state can be formulated following a procedure similar to Faleskog et al. (1998) and Kim et al. (2004). For given values of T and θ, a set of ρ_1 and ρ_2 values can be calculated and the boundary conditions can be imposed according to the nonlinear constraint equations. Kim (2004) provides details of how the boundary conditions are prescribed. In the calculations performed in this section, it is assumed that $\Sigma_2 \geqslant \Sigma_3 \geqslant \Sigma_1$. This assumption results in the Lode angle in the range of $-30° \leqslant \theta \leqslant 30°$.

Fig. 5(a) shows a 1/8-symmetric finite element model for a cubic RMV containing a spherical void and Fig. 5(b) shows the three-dimensional stress state applied on the RMV. The material flow properties used in the finite element analyses represent a typical aluminum alloy, $E = 70.4$ GPa, $\nu = 0.3$, $\sigma_0 = 345$ MPa and $N = 0.14$. The initial void volume fraction is taken as $f_0 = 0.02$. The initial size of the RMV is defined as $X_0 \times X_0 \times X_0$ and the deformed lengths in the x-, y- and z-directions are represented by X, Y and Z, respectively

An axisymmetric loading is considered first, where $\Sigma_2 \geqslant \Sigma_1 = \Sigma_3$ ($\theta = -30°$). Fig. 6(a) shows the variation of X with the macroscopic effective strain (E_e) of the RMV. As loading continues, X gradually decreases. But when the deformation reaches a certain level, X stops decreasing and remains at a constant value. This implies that further deformation takes place in a uniaxial straining mode, which corresponds to flow localization in the ligament between adjacent voids. The shift to a macroscopic uniaxial strain state indicates the onset of void coalescence. Detailed explanation of the uniaxial straining mode can be found in references Koplik and Needleman (1988) and Kim et al. (2004). Here we use E_c to denote the macroscopic effective strain at the onset of void coalescence.

The macroscopic effective stress versus effective strain curve, Fig. 6(b), provides an overview of the competition between matrix material strain hardening and porosity induced softening. As deformation progresses, a maximum effective stress is reached (indicated by the filled circle), and then Σ_e decreases as strain hardening of matrix material is insufficient to compensate for the reduction in ligament area caused by void growth. As the macroscopic effective strain reaches E_c (indicated by the open circle), a rapid drop in macroscopic effective stress occurs. As expected, both the peak stress value and the value of E_c decrease with the stress triaxiality ratio T, reflecting the decrease of ductility.

Most engineering materials contain more than one populations of inclusions and/or second-phase particles. During the void coalescence process, secondary voids nucleate in the ligament between enlarged primary voids and rapid growth and coalescence of these secondary voids accelerates the final ligament separation. Faleskog

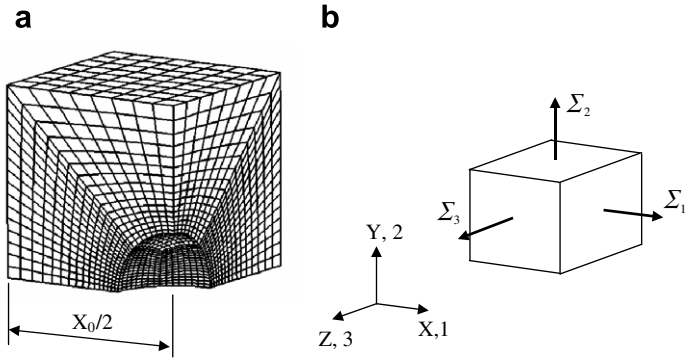

Fig. 5. (a) A one-eighth symmetric finite element mesh for the RMV containing a centered, spherical void. (b) The stress state applied on the RMV.

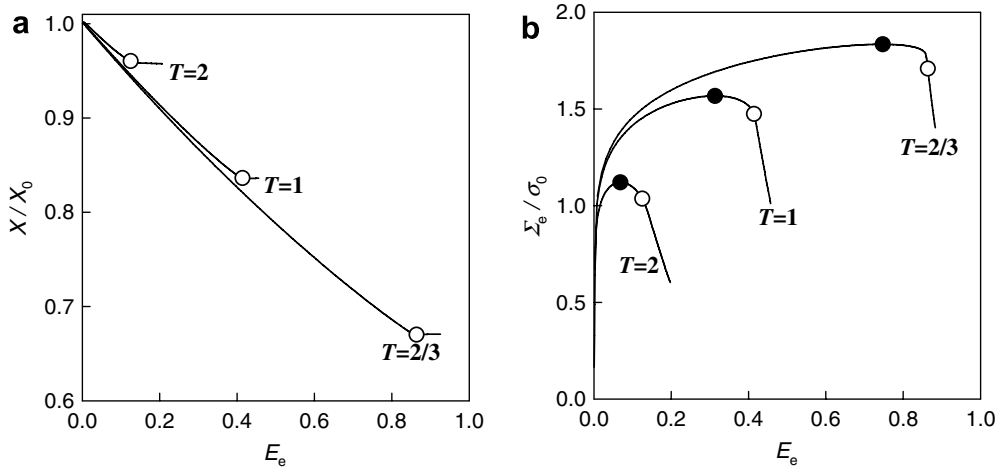

Fig. 6. (a) Variation of the deformed cell width in x-direction with the macroscopic true effective strain of the cell revealing the shift to uniaxial straining. (b) Macroscopic true effective stress versus true effective strain of the void-containing RMV displaying the macroscopic softening. Here the axisymmetric loading is considered so that $E_{xx} = E_{zz} = \ln(X) - \ln(X_0)$, $E_{yy} = \ln(Y) - \ln(X_0)$ and $E_e = 2/3\|E_{yy} - E_{xx}\|$.

and Shih (1997) conducted 2D analysis of void coalescence where both primary and secondary voids are represented using a refined finite element mesh. Here we assume nucleation of the secondary voids is plastic strain controlled and the nucleated voids are smeared in the material. It is further assumed that void nucleation follows a normal distribution as suggested by Chu and Needleman (1980). The GT porous plasticity model (Gurson, 1977; Tvergaard, 1981, 1982) is used to describe the material behavior after void nucleation and the f^* function introduced by Tvergaard and Needleman (1984) is used to account for the coalescence of secondary voids and its effect on material failure. Parameters similar to those used by Tvergaard and Needleman (1984) are employed to describe the nucleation, growth and coalescence of secondary voids. These parameters are chosen just for the purpose of demonstrating the effect of secondary voids on material failure. No attempt is made to represent the actual physical values.

Fig. 7 compares the macroscopic effective stress versus effective strain curves between models including and not including secondary voids. Here several values of stress triaxiality ratio, $T = 1/3$, $2/3$, 1, 1.5 and 2, are

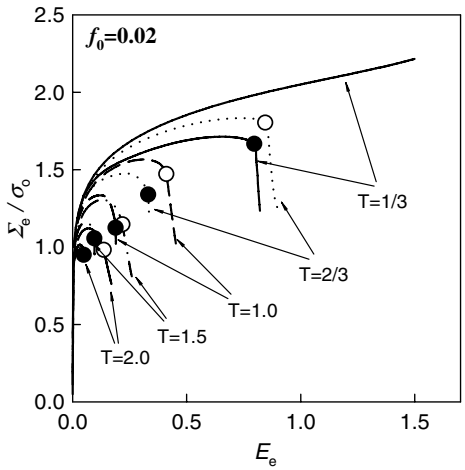

Fig. 7. Comparison of the macroscopic effective stress versus effective strain curves between models including and not including secondary voids. The material properties are $E = 70.4$ GPa, $\nu = 0.3$, $\sigma_0 = 345$ MPa and $N = 0.14$, and the parameters for nucleation of secondary voids are $f_N = 0.04$, $\varepsilon_N = 0.1$ and $s_N = 0.05$.

considered. The open circles denote the onset of coalescence for models where secondary voids are not taken into account. The filled circles represent the onset of coalescence for models where nucleation, growth and coalescence of secondary voids are accounted for. It is clear that secondary voids significantly accelerate the void coalescence process. It is worth noting that, for cases having very low stress triaxiality, e.g., $T = 1/3$, coalescence cannot occur without secondary voids.

The calculations presented above only consider the case where the macroscopic stress state subjected by the RMV is axisymmetric, i.e., $\Sigma_2 \geqslant \Sigma_1 = \Sigma_3$ ($\theta = -30°$). However, as shown in Kim et al. (2004), the Lode angle has significant effect on void growth and coalescence and material failure. Fig. 8 shows the variation of E_c as a function of T and θ: E_c decreases with T but increases with θ. It is interesting to note that the curves for $\theta = -30°$, $-15°$ and $0°$ are very close, which suggests that E_c can be approximated as a function of only T when the Lode angle takes values in this range.

After conducting a series of parameter studies, the following general conclusions can be made about E_c: (1) E_c decreases as T increases, and the dependency of E_c on T is more pronounced in the low stress triaxiality range but saturates as T increases to higher level; (2) E_c increases with θ in the range $-30° \leqslant \theta \leqslant 30°$, but the change in E_c becomes less sensitive to θ when $-30° \leqslant \theta \leqslant 0°$; (3) E_c decreases with f_0, the initial volume fraction of the primary void; (4) nucleation, growth and coalescence of secondary voids accelerate the ligament failure process and reduce E_c; and (5) E_c increases with W_0, the aspect ratio of the primary void. For a given material, the failure criterion can also be expressed as the critical void volume fraction (f_c) or the critical ligament reduction ratio (χ_c) as a function of T and θ.

Results displayed in Fig. 8 can be represented as 3D plots as shown in Fig. 9. The surface representing function $E_c(T,\theta)$ is referred to as the failure surface. Fig. 9(a) and (b) display the failure surfaces obtained for the two cases, $f_0 = 0.02$ with and without secondary voids, respectively. Therefore, a ductile failure criterion for a given material can be established as

$$E_e = E_c(T,\theta) \tag{3}$$

where E_e denote the macroscopic effective strain of the RMV. The RMV fails when E_e reaches a critical value dependent of its stress state characterized by T and θ.

With Σ_2 being the major stress component, Fig. 9 shows only a portion of the failure surface for the range of $-30° \leqslant \theta \leqslant 30°$, i.e., $\Sigma_2 \geqslant \Sigma_3 \geqslant \Sigma_1$. For the case of $\Sigma_2 \geqslant \Sigma_1 \geqslant \Sigma_3$ (corresponding to the range of Lode angle $-90° \leqslant \theta \leqslant -30°$), the failure surface is just a mirror image of the portion shown in Fig. 9. Fig. 10(a) shows a sketch of the failure surface for the range of $-90° \leqslant \theta \leqslant 30°$ where θ covers a 120° span on the π-plane. This includes all possible stress states of which Σ_2 is the major stress component.

The stress state for every RMV in a specimen can be different, each corresponding to a set of (T,θ) values. Even for the same RMV, the values of (T,θ) may change during the loading history. Fig. 10(b) shows a

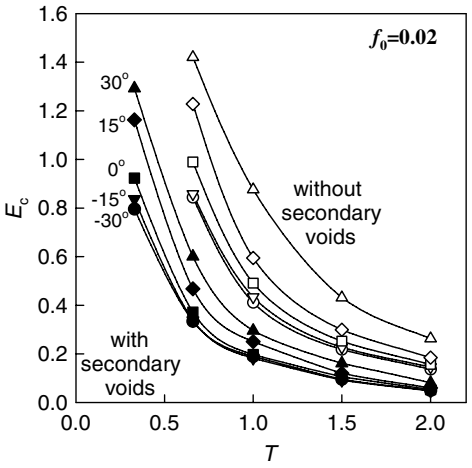

Fig. 8. Variation of E_c as a function of T and θ.

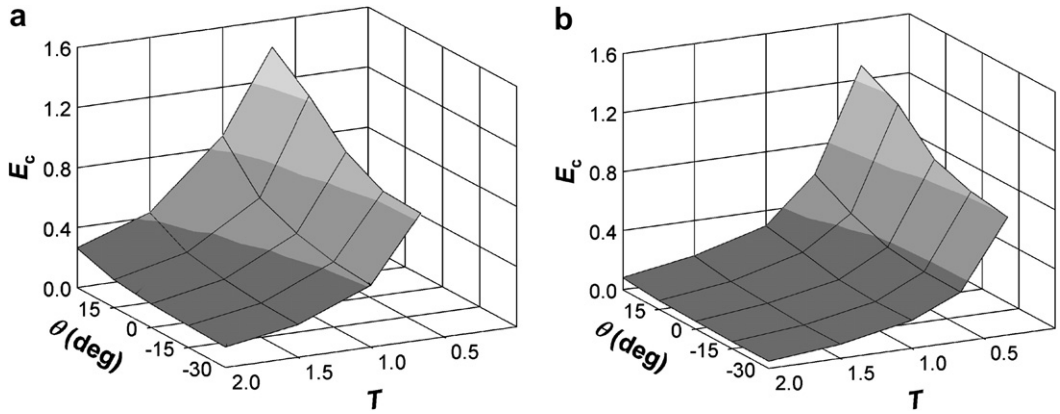

Fig. 9. Material failure surface in terms of E_c as a function of T and θ. (a) $f_0 = 0.02$ and no secondary voids, (b) $f_0 = 0.02$ with secondary voids.

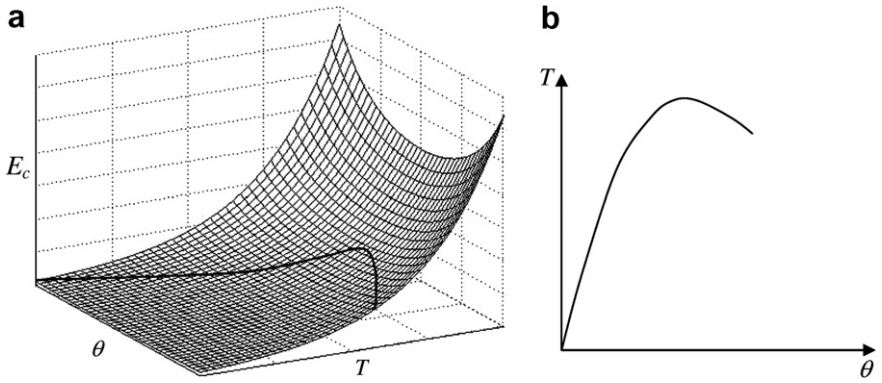

Fig. 10. (a) A sketch of the failure surface $E_c(T,\theta)$ when Σ_2 is the major stress component. (b) A postulated relationship between T and θ.

postulated relationship between T and θ. For each point on the T versus θ curve, there is a corresponding point on the failure surface indicating the failure strain E_c for this stress state. A locus of failure strain is shown in Fig. 10(a).

Bao and Wierzbicki (2004) conducted a series of experiments including upsetting tests, shear tests and tensile tests of different specimens. The test results reveal a non-monotonic relationship between the failure strain and the stress triaxiality. The E_c versus T curve has cusps. This phenomenon has been noticed previously, e.g., Werner and Gese (2003) reported that fracture strain under equi-biaxial tension ($T = 2/3$) is larger that the fracture strain under plane stress ($T = 1/\sqrt{3}$). These results cannot be explained by conventional wisdom of failure strain monotonically decreasing with the increase of stress triaxiality. Using the idea of failure strain dependent of both the stress triaxiality and the Lode angle and with the aid of the failure surface as sketched in Fig. 10, these experimental results can be easily explained.

A similar failure surface was proposed by Wierzbicki and Xue (2005), expressing the fracture strain as a function of both the first and third stress invariants. The features of Wierzbicki and Xue's failure surface are similar to what was described above because one can easily relate the third stress invariant to the Lode angle.

2.4. Fracture toughness

Macroscopic crack initiation is said to have occurred upon coalescence of the growing voids with the crack tip. For the discrete void model described in Section 2.1, it is easier to use the critical ligament reduction ratio

(χ_c) as the failure criterion (Kim et al., 2004; Gao et al., 2005). Here the ligament reduction ratio is defined as the ratio of the current ligament length to the initial ligament length on the crack plane. Readers are referred to Kim et al. (2004) and Gao et al. (2005) for detailed discussion on the critical ligament reduction ratio. Similar to E_c, χ_c also depends on the stress triaxiality and the Lode parameter. Construction of the function $\chi_c(T,\theta)$ for various initial relative void spacing, void shape and void volume fraction follows the same analysis procedures as described in Section 2.3. The fracture initiation toughness (J_{Ic}) is determined as the applied J-value when the reduction of the ligament length between the first void and the crack tip reaches the critical ratio χ_c.

Our results reveal that J_{Ic} decreases with increasing f_0. For the same value of f_0, J_{Ic} is highest when the initial void shape is prolate and lowest when the initial void shape is oblate. Existence of the second row voids and change of void pattern do not result in noticeable difference in J_{Ic}. However, the initial relative void spacing has significant effect on J_{Ic}. Fig. 11 shows the effects of the initial relative void spacing, void pattern, void shape and void volume fraction on the fracture initiation toughness of a structural steel having an intermediate strength and moderate strain hardening. (Here the material properties used in finite element analyses are $E = 200$ GPa, $v = 0.3$, $\sigma_0 = 600$ MPa and $N = 0.1$.) These results can be used to explain why various degrees of fracture toughness anisotropy are observed in industrial alloys.

To model crack growth, the ligament nodes on the symmetry plane are released when the ligament reduction ratio reaches the critical value χ_c. This is done in two steps. First, the analysis is stopped when the critical ligament reduction ratio is reached and a restart file is written. Next, the analysis is restarted with the ligament nodes on the symmetry plane being released. A sudden release of the reaction forces at the ligament nodes

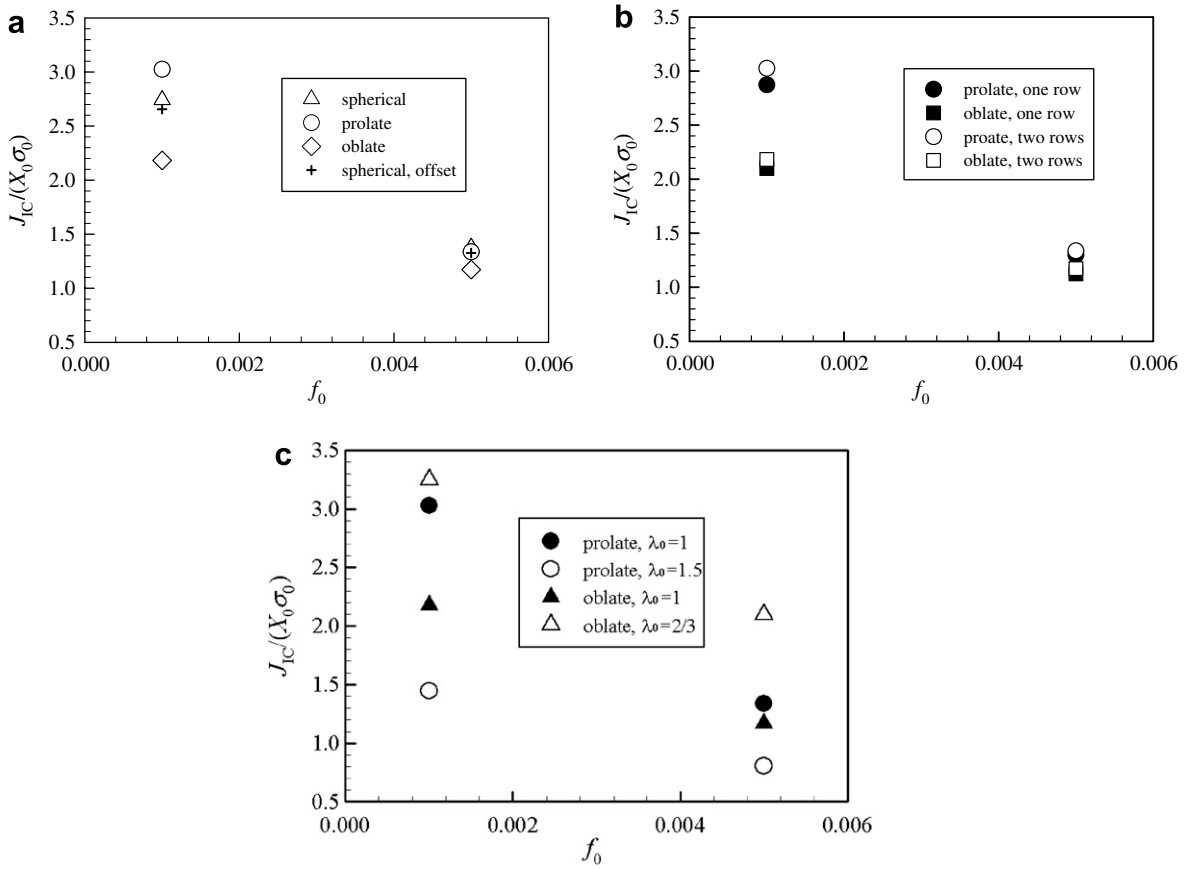

Fig. 11. (a) Predicted dependence of the fracture initiation toughness on the initial void volume fraction and void shape ($\lambda_0 = 1$). (b) Comparison of the predicted fracture initiation toughness values using models containing two rows of voids with those using models containing one row of voids ($\lambda_0 = 1$). (c) Effect of the initial relative void spacing on fracture initiation toughness.

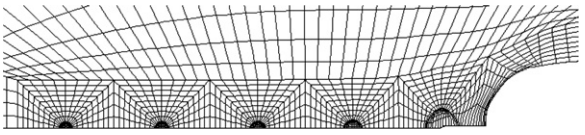

Fig. 12. Crack growth by releasing ligament nodes.

causes numerical instability and therefore, several increments are needed to step down the reaction forces to zero. The deformed mesh immediately following the release of the nodal reaction forces of the first ligament is shown in Fig. 12. Since the reaction forces, which ensure plastic deformation of the ligament, are removed, a large portion of the released ligament experiences elastic unloading with only the weakest region undergoing severe deformation. As the applied load (J) increases, the next ligament reaches the critical reduction ratio and the ligament nodes on the symmetry plane are released. The process continues and the crack front moves forward. The crack growth resistance curve can be obtained by plotting the value of J at which each ligament reaches the failure criterion versus the amount of crack length increase.

3. A numerical approach to predict extensive ductile crack growth

The explicit approach described above provides an effective method for parameter studies to reveal the trends of fracture toughness. However, this approach cannot be applied to predict extensive crack extension in structural components due to the limitation of the current computational power. In this section, we describe a computational approach based on a porous plasticity model and apply it to predict crack propagation in thin panels of a 2024-T3 aluminum alloy. The idea is similar to the computational cell approach used by Xia and Shih (1995) and Gao et al. (1998a,b). The fracture process zone is modeled using a layer of void-containing cell elements and the GLD model is used to describe the void growth process. The onset of coalescence is defined using the criterion developed in Section 2.3, i.e., $E_e = E_c(T, \theta)$, where E_e represents the macroscopic effective strain of the cell. The post-coalescence behavior is modeled using an approach similar to that of Tvergaard and Needleman (1984). Finally the numerical approach is applied to predict crack growth in thin panels of a 2024-T3 aluminum alloy. The expression for E_c is calibrated using experimental data and the calibrated computational model is applied to predict crack extension in fracture specimens having various geometries and subjected to different loading conditions. The numerical predictions are compared with experimental measurements.

3.1. Modeling the void growth process

Because the fracture specimens contain non-spherical voids, we adopt the GLD porous plasticity model (Gologanu et al., 1993, 1994, 1995) to describe the void growth behavior and the macroscopic plastic response of the RMV. The void geometry is illustrated in Fig. 3. The yield function of the void-containing material is expressed as

$$\Phi = \frac{C}{\bar{\sigma}^2}\|\boldsymbol{\Sigma}' + \eta\Sigma_h\mathbf{X}\|^2 + 2q(g+1)(g+f)\cosh\left(\kappa\frac{\Sigma_h}{\bar{\sigma}}\right) - (g+1)^2 - q^2(g+f) = 0 \tag{4}$$

where Σ_{ij} are the macroscopic stress components, f represents the void volume fraction, S is the shape parameter defined as $S = \ln(W)$ with $W = R_y/R_x$, and $\bar{\sigma}$ is the yield stress of the matrix material. In Eq. (4), $\|\,\|$ denotes the von Mises norm, $\boldsymbol{\Sigma}'$ is the deviatoric stress tensor, Σ_h is the generalized hydrostatic stress defined as $\Sigma_h = \alpha_2(\Sigma_{xx} + \Sigma_{zz}) + (1-\alpha_2)\Sigma_{yy}$, $\mathbf{X} = (2/3)e_y \otimes e_y - (1/3)e_x \otimes e_x - (1/3)e_z \otimes e_z$, where $(\boldsymbol{e}_x, \boldsymbol{e}_y, \boldsymbol{e}_z)$ is an orthogonal basis with $\boldsymbol{e}_y$ parallel to the axisymmetric axis of the void, and $\otimes$ denotes tensor product. The parameters C, η, g, κ and α_2 are functions of f and S and the heuristic parameter q depends on initial void volume fraction, strain hardening exponent of the matrix material, S and the macroscopic stress triaxiality factor T.

The evolution law for f due to void growth is determined by requiring the matrix material to be plastically incompressible and derivations of the evolution equation for S can be found in Gologanu et al. (1993, 1994,

1995). Pardoen and Hutchinson (2000, 2003) and Benzerga et al. (2004) provide detailed descriptions and formulation about the GLD model. Kim and Gao (2005) developed a generalized approach to formulate the consistent tangent stiffness for complicated plasticity models. Using this approach, we implemented the GLD model in ABAQUS via a user subroutine. See Kim and Gao (2005) for details of the numerical implementation of the GLD model.

3.2. Onset of coalescence

The GLD model provides a constitutive relation to describe void growth and the associated macroscopic softening of the cell element. It accounts for the evolution of both void shape and void volume fraction. However, the GLD model does not supply the stress–strain relation during the void coalescence process. Therefore it is necessary to introduce a criterion for the onset of coalescence and an equation to govern the cell behavior in the post-coalescence regime.

In developing engineering models for ductile crack growth, a critical void volume fraction (f_c) is often used to predict the onset of the final void coalescence process and a linear traction versus cell elongation relationship to describe the post-coalescence regime (Xia and Shih, 1995; Xia et al., 1995; Gao et al., 1998b). This approximation of the coalescence process greatly simplifies the numerical modeling of ductile fracture. Unfortunately, as shown by Kim et al. (2004), f_c is not a material constant. It varies sensitively with material flow properties, initial void volume fraction, as well as the triaxial stress state of the cell. Moreover, in cases where the stress triaxiality is very low, e.g., near the free surface of the specimen or in a very thin specimen, the void volume fraction does not tend to increase much. Sometimes it never reaches the critical void volume fraction even in an unrealistically large deformation. The (constant) critical void volume fraction criterion cannot be applied in this situation.

In this study, we adopt the coalescence criterion developed in Section 2, e.g., coalescence initiates when the macroscopic effective strain (E_e) of the cell reaches the triaxiality and Lode angle dependent critical value (E_c).

3.3. A computational approach for the post-coalescence process

We adopt the f^* function, introduced by Tvergaard and Needleman (1984), to account for the effects of rapid void coalescence at failure. After E_e reaches E_c, f is replaced by f^* in the GLD model, where

$$f^* = \begin{cases} f, & f \leqslant f_c \\ f_c + K(f - f_c), & f > f_c \end{cases} \tag{5}$$

In Eq. (5), f_c is the void volume fraction at $E_e = E_c$, $K = (f_u - f_c)/f_c$, and f_u is the f^* value at zero stress. For prolate void, $f_u = 1/q$, and for oblate void, $f_u = (1 + g - gq)/q$. Since AQAQUS/Standard does not provide an element removal procedure, a modification to Eq. (5) is needed for numerical stability. Eq. (5) is employed until $f^* = 0.99 f_u$. Then an exponential function is used such that f^* gradually approaches to f_u (but can never reach f_u).

3.4. Simulation of crack growth in thin panels of a 2024-T3 aluminum alloy

The numerical approach described above is applied to predict ductile crack growth in thin aluminum panels. Dawicke and Newman (1997, 1998), and Dawicke et al. (1999) performed extensive fracture tests on thin panels of a 2024-T3 aluminum alloy including tests of C(T), M(T), and multi-site damage (MSD) specimens with crack planes in both the LT and TL orientations. Fig. 13 shows the fracture specimens. The reported data for these tests are mostly for LT specimens and some of them have been analyzed by Gullerud et al. (1999) using a Crack Tip Opening Angle (CTOA) criterion to govern crack growth and by Arun Roy and Dodds (2001) and Roychowdhury et al. (2002) using cohesive elements to model crack propagation. The test data of our interest are from LT specimens with a sheet thickness of 2.3 mm. The specimens have very stiff guide plates (coated with Teflon tape) to constrain out-of-plane (buckling) displacements. In the L orientation, the 2024-T3 sheet material used in the experiments has a yield stress of 345 MPa, Young's Modulus of 71.3 GPa,

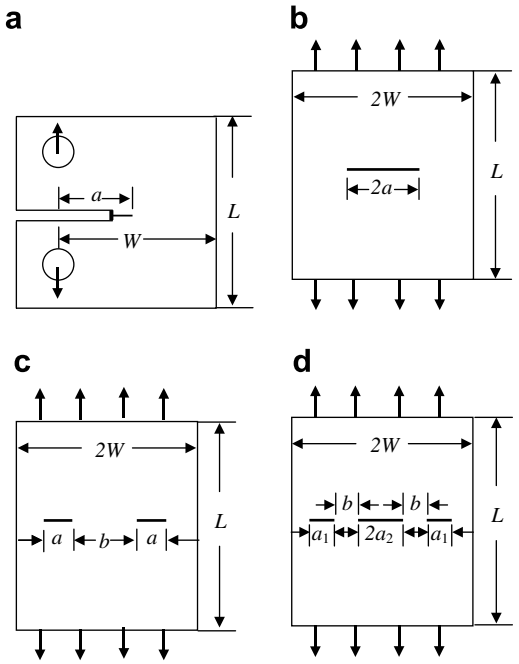

Fig. 13. Fracture specimens: (a) C(T) specimen, (b) M(T) specimen, (c) MSD specimen containing two cracks, (d) MSD specimen containing three cracks.

and Poisson's ratio of 0.3. Quantitative metallographic analyses were performed to determine the inclusion volume fraction, shape and average spacing. It is found that the inclusion volume fraction (f_0) is approximately 0.02, the average spacing between inclusions in the LT plane is about 50 μm, and in LT specimens, the inclusions can be approximated as prolate spheroids with $W_0 = 4$. Our finite element analyses use the measured, unaxial true stress versus logarithmic strain curve.

3.4.1. Model calibration

To predict crack growth, the function $E_c(T, \theta)$ needs to be determined. The results presented in Section 2 suggest that E_c is not sensitive to θ when θ is in the range $-30° \leqslant \theta \leqslant 0°$. We perform finite element analyses of the fracture specimens considered in this study and find the θ-values of the representative material volumes ahead of the crack front are in the range of $-15° \leqslant \theta \leqslant 0°$. Therefore, we treat E_c as a function of T only. This greatly simplifies the calibration process. Based on the results presented in Section 2, we assume

$$E_c = \alpha(T)^{\beta} \tag{6}$$

where α and β are two parameters need to be calibrated using experimental data. A recent study by Bao (2005) supports the power-law form of $E_c(T)$ function defined by Eq. (6). Bao conducted an experimental and numerical study of ductile failure of a 2024-T351 aluminum alloy using different tensile specimens including flat specimens, smooth round bars, notched bars and flat-grooved plates and found that the equivalent strain at failure versus the average stress triaxiality can be characterized by a function in the form of Eq. (6).

Two data points are needed to determine α and β. The uniaxial tension test provides one point, $T = 1/3$ and $E_c = 0.182$. The uniaxial tension specimen displayed very little amount of necking at failure. So the triaxiality ratio should be very close to 1/3. Substitution of these values of T and E_c into (6) results in $\alpha = 0.182(3)^{\beta}$. The next step of the calibration process seeks to match the model predicted load versus crack propagation curve with the experimental measurements for the C(T) specimen. This step entails several finite element crack growth analyses of the C(T) specimen using different values of β.

The C(T) specimen has a width of 150 mm with $a/W = 0.33$, where a represents the initial crack length and W represents the specimen width. Due to symmetry, only 1/4 of the specimen needs to be modeled. Fig. 14

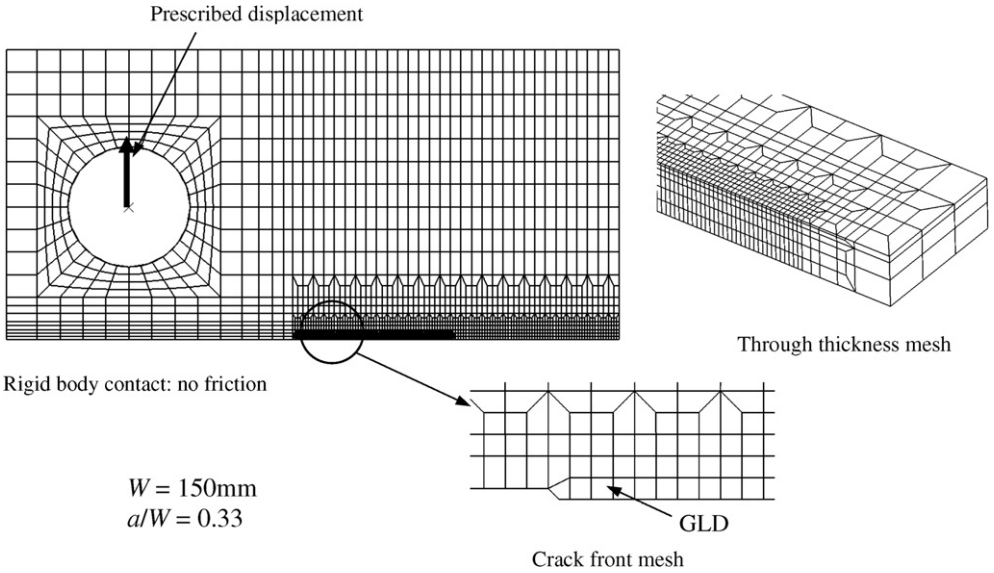

Fig. 14. A quarter-symmetric finite element mesh for the C(T) specimen. The mesh near the crack front has six layers with varying thickness to capture the stress gradient in the thickness direction. The elements directly ahead of the crack front have uniform in-plane dimensions ($L_e = 50$ μm) and are governed by the GLD model.

shows the quarter-symmetric finite element mesh of the C(T) specimen having 27,400 eight-node, isoparametric solid elements (with reduced integration). The mesh near the crack front has six layers with varying thickness to capture the stress gradient in the thickness direction, where the thickest elements are at the symmetry plane. The elements directly ahead of the crack front have uniform in-plane dimensions ($L_e = 50$ μm) and are governed by the GLD model. All other elements follow J_2 flow plasticity. Loading of the C(T) specimen is controlled by prescribing a displacement on a rigid pin through the hole.

Fig. 15 shows the comparison between the model predicted load versus crack growth curve with the experimental measurements (two sets of experimental data) for different choices of α and β, where the lines represent model predictions and the symbols denote experimental measurements. Here Δa represent the amount of crack growth measured at the free surface. In the numerical model, the propagating crack front is defined by the elements which have reached the failure strain E_c. From Fig. 15, it can be seen that the choice of $\alpha = 0.1$ and $\beta = -0.5451$ (solid line) results in the best fit to the experimental data. Therefore, these values are the calibrated values for α and β and will be used to predict crack growth in other fracture specimens.

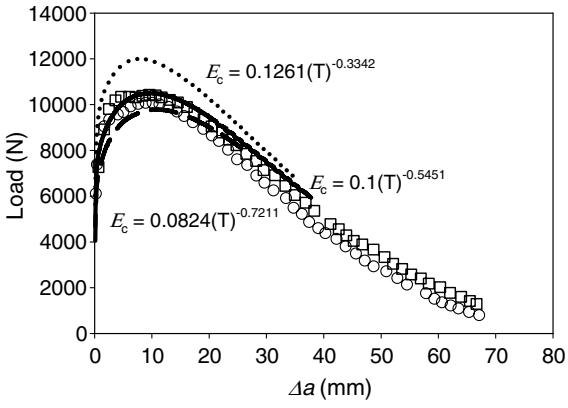

Fig. 15. Comparison of the model predicted load versus crack growth curve with the experimental measured data (symbols) showing the choice of $\alpha = 0.1$ and $\beta = -0.5451$ (solid line) results in a best fit to the experimental data.

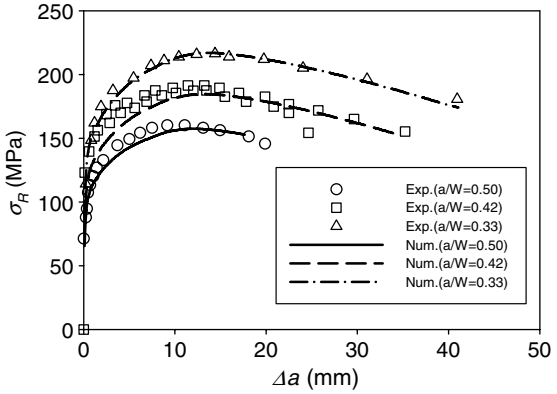

Fig. 16. Comparison of the model predicted load versus crack extension responses (lines) with experimental measurements (symbols).

3.4.2. Prediction of crack growth in M(T) specimens

The calibrated computational model is employed to predict the crack extension behavior of M(T) specimens. Three M(T) specimens with a/W ratios of 0.33, 0.42 and 0.5 are analyzed. The element size and arrangement in the region near the crack front are kept the same as used in the C(T) specimen. The nominal remote stress, σ_R, characterizes the loading for these specimens. Fig. 16 compares the computed load versus crack extension responses with experimental measurements, showing very good agreement for all three cases.

3.5. Prediction of crack growth in MSD specimens

We now apply the calibrated computational model to predict crack growth in MSD specimens. The presence of MSD can significantly influence the residual strength of a structure. Fig. 17 compares the computed load versus crack extension responses with experimental measurements for a MSD specimen containing three cracks as shown in Fig. 13(d). This specimen has the same width as the M(T) specimens considered above, $W = 300$ mm. The half-length of the center crack is $a_2 = 50$ mm. The two lead cracks have the same length $a_1 = 12.5$ mm. The tip-to-tip distance between the lead crack and the center crack is $b = 12.5$ mm. The model prediction captures accurately the load versus crack extension curve. The cusp on the predicted load versus crack extension curve corresponds to the point when the lead crack and the center crack link up. The center crack in this specimen starts to grow at about the same applied stress level as the M(T) specimen with $a/W = 0.33$. But in the MSD specimen, the center crack and lead cracks link up and fail at a significantly lower load than the single crack specimen.

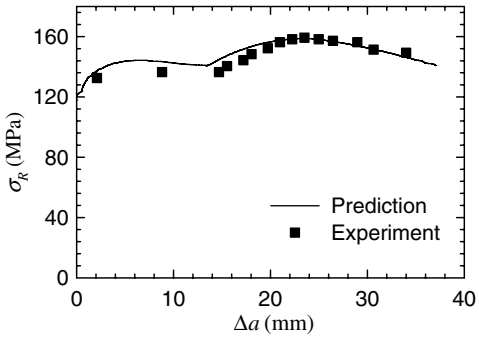

Fig. 17. Comparison of the model predicted load versus crack extension responses (line) with experimental measurements (symbols) for a MSD specimen containing three cracks.

The computational model is also applied to predict crack growth in a series of MSD specimens containing three cracks but with various values of b. Fig. 18 compares the predicted and measured loads at which the lead cracks and the center crack link up. The computed values and experimental data agree very well.

Fig. 19 compares the computed load versus crack extension curve with experimental records for a MSD specimen containing two cracks as shown in Fig. 13(c). For this specimen, $W = 300$ mm, $a = b = 50$ mm. Fig. 20 compares the computed and measured crack link up loads for a series of two-crack specimens with various b-values. Again very good agreements are found between the model predictions and the experimental measurements. This further verifies the proposed computational approach.

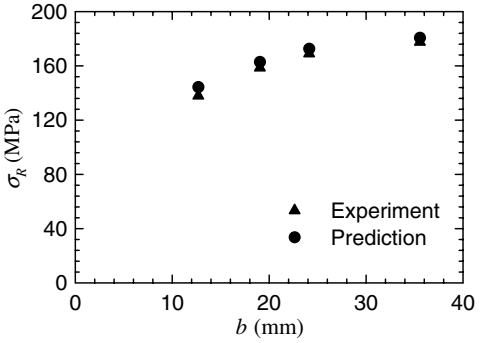

Fig. 18. Comparison of the predicted and measured loads at which the lead cracks and the center crack link up for a series of MSD specimens containing three cracks.

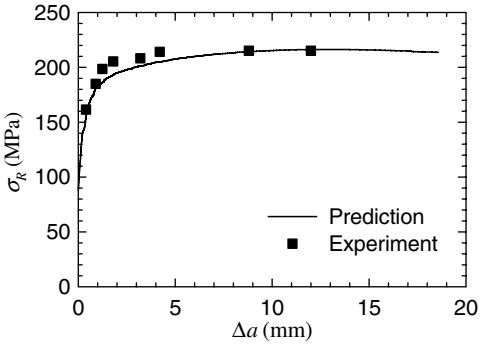

Fig. 19. Comparison of the model predicted load versus crack extension responses (line) with experimental measurements (symbols) for a MSD specimen containing two cracks.

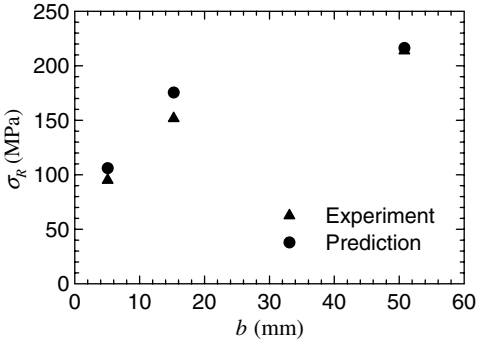

Fig. 20. Comparison of the predicted and measured crack link up loads for a series of MSD specimens containing two cracks.

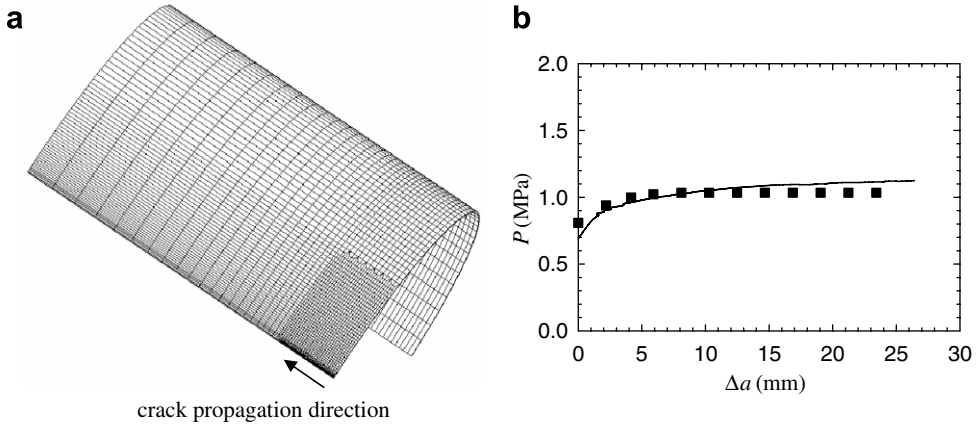

Fig. 21. (a) Finite element mesh of a pressurized cylindrical shell. (b) Comparison of the predicted and measured applied pressure versus crack extension response.

3.5.1. Prediction of crack growth in a pressurized cylindrical shell structure

To study the influence of a crack on the structural response of the transport fuselage structure, Starnes and Rose (1997) conducted a series of pressurized cylindrical shell tests. The cylindrical shells were fabricated from 1 mm-thick 2024-T3 aluminum alloy sheet, with the rolling direction orientated circumferentially. A longitudinal crack is located at the mid-length of the cylindrical shell. Here we apply the above calibrated computational model to predict the crack growth behavior in the pressurized cylindrical shell structure. Although the shell thickness is different from the C(T), M(T) and MSD specimens analyzed above, we assume that the microstructure and flow properties of the material remain the same. The specimen under our consideration has a radius of 230 mm and length of 914 mm. The initial crack length is $a = 25$ mm. Fig. 21(a) shows the finite element mesh of the cylindrical shell. Due to symmetry of the geometry and loading conditions, only a quarter of the shell is modeled. Ten layers of eight-node brick elements are employed in the wall thickness direction. The element dimensions in the crack opening direction and crack growth direction are kept the same as used in the C(T), M(T) and MSD specimens in the crack front region. The pressure load is applied on the inner surface of the shell. Fig. 21(b) shows that the predicted load versus crack growth response agree well with the experimental measurements.

4. Concluding remarks

Two approaches, one uses refined finite elements to represent microvoids in the material and the other uses porous plasticity models to describe the behavior of the void-containing material, are discussed in this paper. A distinct advantage of the first approach is the exact implementation of the void growth behavior. It provides an effective method to study the mechanisms of ductile fracture and to analyze the trends of fracture toughness. With model parameters being properly calibrated, the second approach can be used to predict extensive crack extension in fracture specimens.

Our analyses re-affirm the two distinct void growth mechanisms put forth by Tvergaard and Hutchinson (2002), i.e., void-by-void growth mechanism for materials containing small initial void volume fractions and multiple void interaction mechanism for materials containing large initial void volume fractions. Effects of the initial relative void spacing, void pattern, void shape and void volume fraction are investigated in this study.

In order to simulate crack formation and propagation, a criterion for void coalescence is required. The critical strain at the onset of void coalescence depends on material flow properties and microstructural properties. It also depends on the stress state. Two stress parameters, the stress triaxiality ratio (T) and the Lode angle (θ) can be used to characterize the effect of the macroscopic stress state on the void growth and coalescence process in the representative material volume (RMV). We obtain the failure criterion for the RMV in terms of the

macroscopic equivalent strain (E_c) as a function of T and θ by conducting systematic finite element analyses of the void-containing RMV subjected to different macroscopic stress states. A series of parameter studies are conducted to examine the effects of the shape and initial volume fraction of the primary void and nucleation, growth and coalescence of the secondary voids on the predicted failure surface $E_c(T,\theta)$.

Using the small scale yielding, boundary layer model with discrete voids represented in the crack tip region by refined finite element mesh, the effects of the initial relative void spacing, void pattern, void shape and void volume fraction fracture initiation toughness are investigated. The results can be used to explain the observed fracture toughness anisotropy in industrial alloys. With the aid of a node-release technique, crack growth and fracture resistance curve can be predicted.

Finally a numerical approach is proposed to predict extensive ductile crack growth in structural materials. The computational model is applied to predict crack growth in thin panels of a 2024-T3 aluminum alloy, where the GLD porous plasticity model is used to describe the void growth process and a f^* function is employed to account for rapid material failure in the post-coalescence process. For the specimens considered in this study, it is found that the Lode angles of the void-containing cell elements are in the range of $-15° \leqslant \theta \leqslant 0°$. Consequently, the critical strain at the onset of void coalescence can be approximated as a function of the stress triaxiality ratio only and a calibration procedure to determine $E_c(T)$ is presented. The calibrated computational model accurately predicts crack extension in a series of fracture specimens having various initial crack configurations, including the compact tension specimen, middle crack tension specimens, multi-site damage specimens and the pressurized cylindrical shell specimen.

Acknowledgement

This research was made possible through research funding provided by the Office of Naval Research (N00014-02-1-0423) and by the Ohio Board of Regents.

References

ABAQUS/Standard User's Manual, Version 6.2, 2001. Hibbit, Karlsson and Sorensen Inc.

Anderson, T.L., 1994. Fracture Mechanics: Fundamentals and Applications, second ed. CRC Press, Boca Raton.

Aravas, N., McMeeking, R.M., 1985a. Finite element analysis of void growth near a blunting crack tip. J. Mech. Phys. Solids 33, 25–49.

Aravas, N., McMeeking, R.M., 1985b. Microvoid growth and failure in the ligament between a hole and blunt crack tip. Int. J. Fract. 29, 21–38.

Arun Roy, Y., Dodds, R.H., 2001. Simulation of ductile crack growth in thin aluminum panels using 3D surface cohesive elements. Int. J. Fract. 110, 21–45.

Bao, Y., 2005. Dependence of ductile crack formation in tensile tests on stress triaxiality, stress and strain Ratios. Eng. Fract. Mech. 72, 505–522.

Bao, Y., Wierzbicki, T., 2004. On fracture locus in the equivalent strain and stress triaxiality space. Int. J. Mech. Sci. 46, 81–98.

Benzerga, A.A., 2002. Micromechanics of coalescence in ductile fracture. J. Mech. Phys. Solids 50, 1331–1362.

Benzerga, A.A., Besson, J., Pineau, A., 2004. Anisotropic ductile fracture – Part II: Theory. Acta Mater. 52, 4639–4650.

Bridgman, P.W., 1952. Studies in Large Plastic Flow and Fracture. McGraw-Hill Inc.

Chu, C.C., Needleman, A., 1980. Void nucleation effects in biaxially stretched sheets. J. Eng. Mater. Tech. 102, 249–256.

Dawicke, D.S., Newman, J.C., 1997. Evaluation of fracture parameters for prediction residual strength of multi-site damage cracking. In: Proceedings from the First Joint NASA/FAA/DoD Conference on Aging Aircraft, pp. 1307–1326.

Dawicke, D.S., Newman, J.C., 1998. Residual strength predictions for multiple site damage cracking using a three-dimensional finite element analysis and a CTOA criterion. In: Panontin, T.L., Sheppard, S.D. (Eds.), Fracture Mechanics: vol. 29th, ASTM STP 1321, Philadelphia, PA, pp. 815–829.

Dawicke, D.S., Newman, J.C., Starnes, J.H., Rose, C.A., Young, R.D., Seshadri, B.R., 1999. Residual strength analysis methodology: laboratory coupons to structural components. In: Proceedings of the Third Joint NASA/FAA/DoD Conference on Aging Aircraft, September 20–23, Albuquerque, New Mexico.

Faleskog, J., Shih, C.F., 1997. Micromechanics of Coalescence – I. Synergistic effects of elasticity, plastic yielding and multi-size-scale voids. J. Mech. Phys. Solids 45, 21–50.

Faleskog, J., Gao, X., Shih, C.F., 1998. Cell model for nonlinear fracture analysis – I. Micromechanics calibration. Int. J. Fract. 89, 355–373.

Gao, X., Kim, J., 2006. Modeling of ductile fracture: significance of void coalescence. Int. J. Solids Struct. 43, 6277–6293.

Gao, X., Faleskog, J., Shih, C.F., 1998a. Cell model for nonlinear fracture analysis – II. Fracture-process calibration and verification. Int. J. Fract. 89, 375–398.

Gao, X., Faleskog, J., Dodds, R.H., Shih, C.F., 1998b. Ductile tearing in part-through cracks – experiments and cell-model predictions. Eng. Fract. Mech. 59, 761–777.

Gao, X., Wang, T., Kim, J., 2005. On ductile fracture initiation toughness: effects of void volume fraction, void shape and void distribution. Int. J. Solids Struct. 42, 5097–5117.

Garrison Jr., W.M., Moody, N.R., 1987. Ductile fracture. J. Phys. Chem. Solids 48, 1035–1074.

Gologanu, M., Leblond, J.B., Devaux, J., 1993. Approximate models for ductile metals containing nonspherical voids – case of axisymmetric prolate ellipsoidal cavities. J. Mech. Phys. Solids 41, 1723–1754.

Gologanu, M., Leblond, J.B., Devaux, J., 1994. Approximate models for ductile metals containing nonspherical voids – Case of axisymmetric oblate ellipsoidal cavities. J. Eng. Mater. Tech. 116, 290–297.

Gologanu, M., Leblond, J.B., Perrin, G., Devaux, J., 1995. Recent extensions of Gurson's model for porous ductile metals. In: Suquet, P. (Ed.), Continuum Micromechanics. Springer-Verlag, pp. 61–130.

Gullerud, A.S., Dodds, R.H., Hampton, R.W., Dawicke, D.S., 1999. 3D modeling of ductile crack growth in thin sheet metals: computational aspects and validation. Eng. Fract. Mech. 63, 347–374.

Gurson, A.L., 1977. Continuum of ductile rupture by void nucleation and growth: Part I – Yield criteria and flow rules for porous ductile media. J. Eng. Mater. Tech. 99, 2–55.

Hom, C.L., McMeeking, R.M., 1989. Void growth in elastic–plastic materials. J. Appl. Mech. 56, 309–317.

Hutchinson, J.W., Evans, A.G., 2000. Mechanics of materials: top-down approaches to fracture. Acta Mater. 48, 125–135.

Kim, J., 2004. Mechanism based approaches for prediction of ductile fracture. PhD dissertation, The University of Akron.

Kim, J., Gao, X., 2005. A generalized approach to formulate the consistent tangent stiffness in plasticity with application to the GLD porous material model. Int. J. Solids Struct. 42, 103–122.

Kim, J., Gao, X., Srivatsan, T.S., 2003. Modeling of crack growth in ductile solids: a three-dimensional analysis. Int. J. Solids Struct. 40, 7357–7374.

Kim, J., Gao, X., Srivatsan, T.S., 2004. Modeling of void growth in ductile solids: effects of stress triaxiality and initial porosity. Eng. Fract. Mech. 71, 379–400.

Koplik, J., Needleman, A., 1988. Void growth and coalescence in porous plastic solids. Int. J. Solids Struct. 24, 835–853.

Pardoen, T., Hutchinson, J.W., 2000. An extended model for void growth and coalescence. J. Mech. Phys. Solids 48, 2467–2512.

Pardoen, T., Hutchinson, J.W., 2003. Micromechanics-based model for trends in toughness of ductile metals. Acta Mater. 51, 133–148.

Rice, J.R., 1974. Limitations to the small scale yielding approximation for crack tip plasticity. J. Mech. Phys. Solids 22, 17–26.

Roychowdhury, S., Arun Roy, Y., Dodds, R.H., 2002. Ductile tearing in thin aluminium panels: experiments and analyses using large-displacement, 3-D surface cohesive elements. Eng. Fract. Mech. 69, 983–1002.

Ruggieri, C., Panontin, T.L., Dodds, R.H., 1996. Numerical modeling of ductile crack growth in 3-D using computational cell elements. Int. J. Fract. 82, 67–95.

Starnes, J.H., Rose, C.A., 1997. Effects of initial crack length on stable tearing and buckling of selected unstiffened aluminum shells subjected to internal pressure and axial compression. In: Proceedings of the FAA-NASA Symposium on the Continued Airworthiness of Aircraft Structures, DOT/FAA/AR-92/2, pp. 601–626.

Tvergaard, V., 1981. Influence of voids on shear band instabilities under plane strain conditions. Int. J. Fract. 17, 389–407.

Tvergaard, V., 1982. On localization in ductile materials containing spherical voids. Int. J. Fract. 18, 237–252.

Tvergaard, V., Hutchinson, J.W., 2002. Two mechanisms of ductile fracture: void by void growth versus multiple void interaction. Int. J. Solids Struct. 39, 3581–3597.

Tvergaard, V., Needleman, A., 1984. Analysis of the cup-cone fracture in a round tensile bar. Acta Metall. 32, 157–169.

Van Stone, R.H., Cox, T.B., Low Jr., J.R., Psioda, J.A., 1985. Microstructural aspects of fracture by dimple rupture. Int. Met. Rev. 30, 157–179.

Werner, H., Gese, H., 2003. A new comprehensive failure model for crashworthiness simulation – validation for aluminum extrusions. In: EURO PAM 2003, October 16–17.

Wierzbicki, T., Xue, L., 2005. On the effect of the third invariant of the stress deviator on ductile fracture. Technical Report, Impact and Crashworthiness Lab, MIT.

Xia, L., Shih, C.F., 1995. Ductile crack growth – I. A numerical study using computational cells with microstructurally-based length scales. J. Mech. Phys. Solids 43, 233–259.

Xia, L., Shih, C.F., Hutchinson, J.W., 1995. Computational approach to ductile crack growth under large scale yielding conditions. J. Mech. Phys. Solids 43, 389–413.